Journal of Theoretical Biology 409 (2016) 70–85

Contents lists available at ScienceDirect

Journal of Theoretical Biology

journal homepage: www.elsevier.com/locate/yjtbi

The impact of human and vector distributions on the spatial prevalence of malaria in sub-Saharan Africa

Shawn A. Means [a], Robert J. Smith? [b,*]

[a] Auckland Bioengineering Institute, University of Auckland, New Zealand
[b] Department of Mathematics and Faculty of Medicine, The University of Ottawa, Canada

HIGHLIGHTS

- This is one of the few models of malaria to account for spatial distributions.
- We examine the effects of varying the density of structures in malaria-endemic areas, given the diffusive behaviour of mosquitoes.
- We show that the initial distribution of structures is key to reducing the effects of malaria in prevalent areas.

ARTICLE INFO

Article history:
Received 24 August 2015
Received in revised form
1 July 2016
Accepted 23 August 2016
Available online 27 August 2016

Keywords:
Malaria
Reaction-diffusion
Spatial distribution
Mathematical modelling
Infectious dynamics

ABSTRACT

Eradication of malaria from the world in the latter part of the twentieth century proved an elusive, albeit desirable, objective. Unfortunately, resurgence of malarial incidence is currently underway. Key to understanding effective control schemes such as indoor residual spraying (spraying insecticide inside houses to kill the malarial vector mosquitoes) is the impact of spatial distributions for communities exposed to the malarial vector mosquito populations. Densities of human dwellings in small communities vary considerably in regions exposed to larval breeding sites. We extend prior modelling work to explore the spatial impact and diffusive transport of mosquito population densities on various distributions of human populations on relatively small landscape representations. Bistable dynamics of our reaction-diffusion model, which excludes advective transport, suggest two temporal phases for infection. An initial rapid phase occurs during transitions from initial homogeneous or spatially confined infections to peak levels over the course of days, and a relaxation phase develops to a steady state over weeks or months, suggesting successful intervention methods likely require recognising the phase of infection. We further observe a strong dependence of human infection and recovery on distributions of susceptible human populations with some degree of independence from mosquito distributions given an adequate supply of mosquito vectors to sustain infections. A subtle and complex interplay between human dwelling densities, mosquito diffusion and infection rates also emerges. With a sufficiently fast diffusive transport of mosquitoes, our model indicates that relative timescales for infection rates are slower, leading to lower rates of infection. This suggests that, although we here only include diffusive transport, if mosquitoes are subject to rapid enough movement (e.g., wind), communities situated in windy areas are exposed to less infectious risk than those in non-windy areas. This should help to guide intervention strategies with geographical considerations in mind. Our implementation of a reaction-diffusion model here further reveals some issues regarding continuum methods for population and infectious disease models that suggest consideration of discrete spatial methods (e.g., agent-based) for future work.

1. Introduction

The impact of malaria on infected individuals, associated economic effects and social ramifications are profound (Keiser et al., 2004). Infections are estimated to affect 360 million individuals annually (Snow et al., 2005), resulting in millions of deaths per annum (Breman et al., 2004), including significant numbers of sub-Saharan children (Keiser et al., 2004). Nearly half the population of the Earth is at risk from malarial infection (Snow et al., 2005; Lopez et al., 2006; Silué et al., 2008). Although current

* Corresponding author.
E-mail addresses: s.means@auckland.ac.nz (S.A. Means), rsmith43@uottawa.ca (R.J. Smith).

http://dx.doi.org/10.1016/j.jtbi.2016.08.031
0022-5193/

decreases in malaria mortality are encouraging, continued and increased efforts are required to achieve elimination and eradication objectives (Murray et al., 2012).

In the twentieth century, malaria was one of four diseases targeted for eradication (Alyward et al., 2000). The others were smallpox, yellow fever and yaws, a tropical infection of the skin, bones and joints. Only smallpox was successful. Despite being cost-beneficial and having broad societal and political support (Alyward et al., 2000), malaria eradication efforts failed due to a combination of factors including insecticide resistance, economic under-development, non-human primate reservoirs and the discontinuation of DDT as a method of vector control, following publication of "Silent Spring" (Carson, 1962), although we can only speculate as to the effectiveness of more potent historical DDT usage.

Control measures for the malarial transmission vector—the mosquito—include insecticides aimed at either the winged adults or the water-bound larvae; interior or indoor residual spraying (IRS) (Smith? and Hove-Musekwa, 2008); and insecticide-treated nets situated within dwellings (Killeen et al., 2013). IRS and insecticide-treated nets are effective (Macintyre et al., 2006), whereas direct intervention of larval breeding sites and adult vector population controls may have mixed results (Fillinger et al., 2009). Such exterior interventions require further analysis for optimising effectiveness (Killeen et al., 2013; Githeko et al., 2012). All methods are necessarily dependent on key factors of the transmission vector's dynamical dependence on spatial components, including landscape topology, proximity of susceptible populations, population densities and structure types and distributions (Carter et al., 2000; Githeko et al., 2012). Recognition and careful consideration of such spatial features are required for implementing effective control measures; for instance, spatial clustering of malarial risk substantially increases the disease's transmission robustness (Hasibeder and Dye, 1988).

Malaria is strongly associated with location, with disease transmission restricted to a few kilometres from specific mosquito breeding sites (Carter et al., 2000). The clustering of malaria risk has been recognised as a potent factor underlying the robustness of malaria transmission (Hasibeder and Dye, 1988). Conversely, knowledge of locations and individuals at high risk allows specific targeting of intervention measures (Ghebreyesus et al., 2000). It follows that the spatial heterogeneity of landscape, urban/rural population densities and the distribution of structures plays an important role in the control of malaria.

We therefore expand previous modelling efforts studying malarial infectious dynamics to include particular spatial components (Al-Arydah and Smith?, 2011). Of the many spatial ingredients relevant to the infection dynamic, we aim to investigate here the proximity of human populations to mosquito breeding sites (or "birth-zones"), the densities of human dwellings and the distributions of human populations over idealised regions. Our aim is to provide insights into the effects of these spatial aspects on the overall mosquito and human infection dynamic. With an improved grasp on how such spatial inhomogeneities affect the robustness of malarial transmission and persistence, we may in turn calibrate the use of control measures such as larval-breeding-site intervention or IRS into more efficient and potent weapons in an ongoing struggle with such a tenacious disease.

2. Methods

2.1. Geometry

Mosquitoes display distinct spatial distribution heterogeneities —particularly in lowland regions near breeding sites with adequate standing water sources (Githeko et al., 2006). We generalise such spatial relationships between larval breeding sites and adult mosquito distributions near human dwellings from published data into a simplified suite of geometries, initial conditions and birthing regions for our simulations. The proximities of mosquito vectors and larval birth-zones to human dwellings is combined with different clusterings of human dwellings and inter-dwelling distances as extracted from historical data. Of interest here is a particular rural region in Kenya, where we obtain via Google Maps a map of dwellings and their relative locations from 2001 (shown in Fig. 1). We focus on this region since available published data from Zhou et al. (2007) shows spatial distributions of larval and adult mosquito vector densities in this area from 2002 (see Figure 1 from Zhou, et al.). The idealised representation of this rural site as generalised into five distinct distributions of farming regions embedded within surrounding landscapes, as well as various dwelling clusterings, is shown in Fig. 2.

2.2. Reaction-diffusion model

We deploy the model already described in Al-Arydah and Smith? (2011), with some variations for our two-dimensional ($\Omega_r \in \mathbb{R}^2$) spatial problem of interest. This reflects a long heritage of ecological "patch" models but with full diffusion of both humans and mosquitoes (Kierstead and Slobodkin, 1953). The previous model included a system of impulsive PDEs. We do not employ impulsive PDEs here but rather a coupled system of reaction-diffusion PDEs split into exterior (Ω_e) and interior (Ω_i) regimes for all mosquito and human variable representations. We briefly summarise the current version of the model here and refer the reader to the prior work for further details.

The model is a classical susceptible-infected-recovered (SIR) depiction in two spatial domains that represent the extra-dwelling and internal-dwelling spaces. In each domain, the full suite of mosquito (virgin "M" and carrier "N") as well as human (S, I, R) variables are included thus:

$$\begin{aligned}
\frac{\partial M_r}{\partial t} &= D_M\nabla^2 M_r + \frac{1}{A_e}\Lambda_e\left(\vec{x}\right) - \mu_q M_r - A_\beta\beta_m M_r I_r \\
\frac{\partial N_r}{\partial t} &= D_M\nabla^2 N_r - \mu_q N_r + A_\beta\beta_m M_r I_r \\
\frac{\partial S_r}{\partial t} &= D_H\nabla^2 S_r + \frac{1}{A_r}\pi\left(\vec{x}\right) - A_\beta\beta_h S_r N_r + hI_r + \delta R_r - \mu_h S_r \\
\frac{\partial I_r}{\partial t} &= D_H\nabla^2 I_r + A_\beta\beta_h S_r N_r - hI_r - \alpha I_r - \left(\mu_h + \gamma\right) I_r \\
\frac{\partial R_r}{\partial t} &= D_H\nabla^2 R_r + \alpha I_r - \delta R_r - \mu_h R_r,
\end{aligned} \tag{1}$$

where the subscript r indicates the spatial domain where the variable resides and $\vec{x} \in \mathbb{R}^2$. These domains include the "exterior" (e) or "interior" (i) domains, as well as a sub-domain of the external, which we call the "farming" (f) domain; hence we have $r \in \{e, f, i\}$. The farming sub-domain is added for distinction between the domain where humans (S, I, R) are situated in a farming region and where they are not: the extra-farming region where mosquitoes are born but do not encounter humans. Hence we have $\Omega_f \subset \Omega_e$. In our model, it is only within the "farming" region (Ω_f) and interior dwelling region (Ω_i) where moquitoes and humans interact. Note that both non-infected, M, and carrier, N, mosquitoes reside in all three domains, although the interior and exterior varieties are spatially distinct variables separated by the internal dwelling boundary $\partial\Omega_i$.

A term included here yet not in the prior work (Al-Arydah and Smith?, 2011) is the area, A, which provides suitable dimensions and scaling for each domain's spatial extent either for births (A_r) or

Fig. 1. Historical landscape map for the year 2001 from Google Earth. This particular scene corresponds to the 2002 data presented in Figure 1 of Zhou et al. (2007) that depicts clusters of high mosquito larva and adult densities (highlighted in roughly elliptical regions) in this particular area of Kenya: the Iguhu, Kakamega District south of the Yala river. Note the number and variety of dwelling groupings, as well as interdwelling distances. Black bar = 100 m.

infections (A_β). Additionally, our mosquito birth function, $\Lambda_e(\vec{x})$, is spatially inhomogeneous and thus also distinct from the 2011 model; it is further active only for the exterior region Ω_e. We utilise this function to represent a "birth-zone" of larval activity and vary the spatial extent of this birth region to explore its effects on the infection dynamic. It is configured as a Heaviside distribution varying only in one spatial direction (here, x), effectively confining mosquito births to a rectangular strip (e.g., $-300\text{ m} \le x \le x_{bz}$). Steady-state profiles result from the balance between the rectangular region of births and the homogenous death rate, which can be seen in Fig. 4. Each birth-zone variant is described in the Results section below and noted in Table A1. Another novel spatial dependence is via the human births, $\pi(\vec{x})$. $\pi(\vec{x})$ is held to a constant and uniform value at the level given in the parameters table or permitted spatial dependence in a Gaussian-fashion, as noted in the results. Note that the diffusion coefficients for mosquitoes M and N are the same as in Al-Arydah and Smith? (2011) and are identical for each variable and across all domains. The human diffusion coefficients are similarly identical across the human variables (S, I, R) and domains (Ω_f, Ω_i) yet are chosen to represent a vastly slower diffusion scale than the mosquito while not being identically zero as in the 2011 model. These parameter values are also listed in Table A1.

Boundary conditions for the external mosquito variables (M_e and N_e) are Neumann insulation on the external boundary enveloping the exterior domain, which we denote $\partial\Omega_e$, while a linear difference transport flux condition couples the interior and exterior mosquito variables (e.g., N_e and N_i) on the shared boundary between domains Ω_e and Ω_i, denoted $\partial\Omega_i$:

$$\left.\frac{\partial M_r}{\partial \mathbf{n}}\right|_{\partial\Omega_i} = \sigma_r(M_e - M_i) \tag{2}$$

$$\left.\frac{\partial N_r}{\partial \mathbf{n}}\right|_{\partial\Omega_i} = \sigma_r(N_e - N_i). \tag{3}$$

The permeability term σ is varied over simulations to represent the porosity of dwellings (e.g., mud/thatch roof with a high porosity or brick with a low porosity; see Table A1), and the signs adjusted for suitable transport direction depending on the domain (e.g., external or internal, or $r \in e, i$). Note that there is no coupling between the internal and external human variables S_f and S_i, etc.; these variables are completely distinct. The only route of transfer between internal human states (susceptible to infected, say) is via intrusion of an external carrier mosquito, N_e, into a dwelling with the above transport condition (Eq. (3)) converting the external carrier to an internal, or N_i. Note that the farm domain boundary—denoted $\partial\Omega_f$—is diffusively transparent to mosquito variables and simultaneously functions as a Neumann insulation flux condition for the exterior or "farm" region human variables. See Fig. 2 for a schematic depicting these details.

Note that mosquito and human variables occupy different

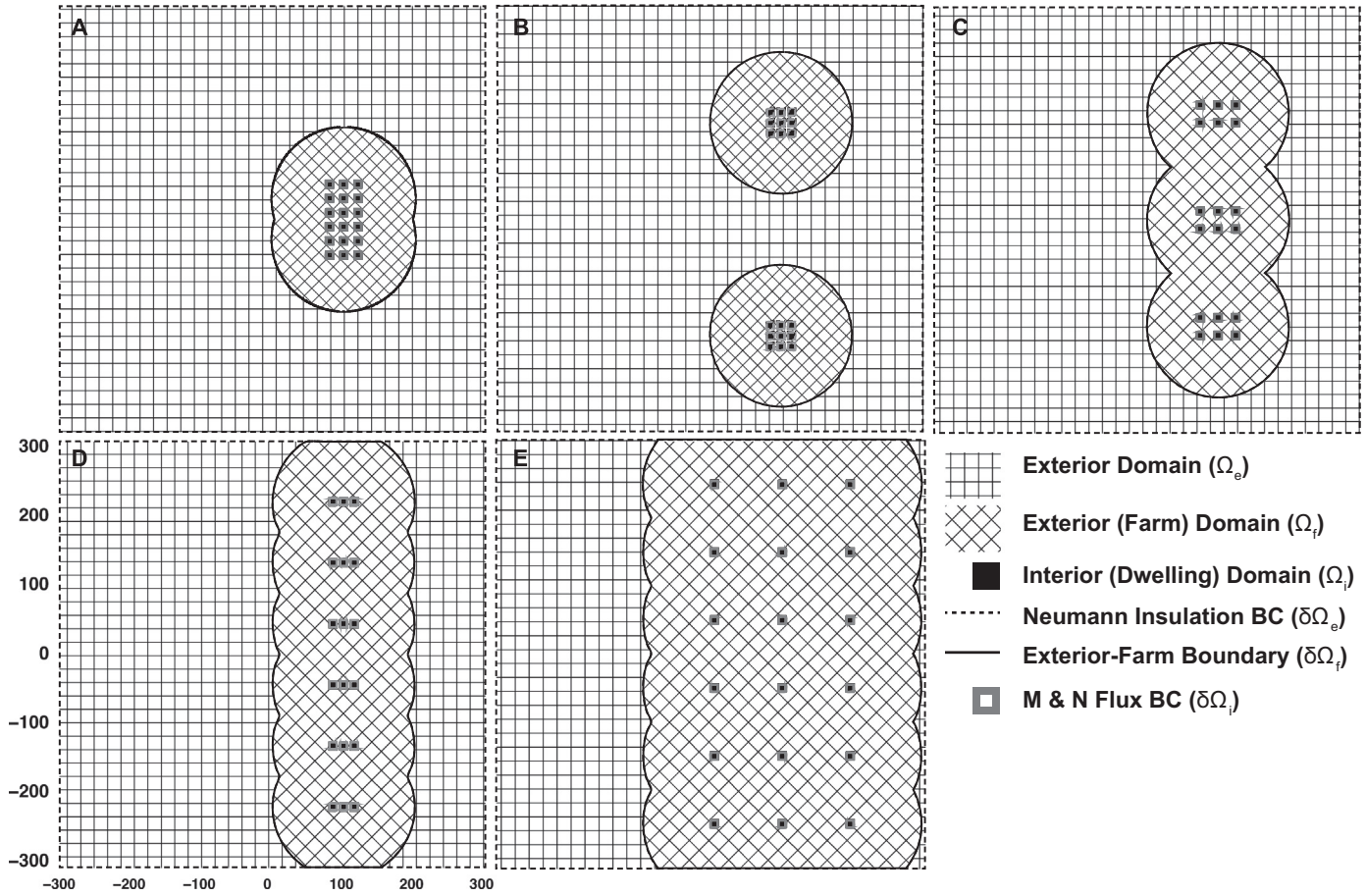

Fig. 2. Geometries (scale: metres). Overall, five square geometries—with identical extents of 600 × 600 m—were employed in our simulations. Each geometry is based on a generalised interpretation of actual dwelling distribution and clustering taken from the historical map data shown in Fig.1. We chose to represent highly clustered dwellings as in panel (A) and sparsely clustered as in (E). Variants of two cluster (B), three (C) and six (D) were included. Each geometry contains 18 dwellings, with the centre column of dwellings aligned at $x=100$ m in each geometry. Clustering variants were further altered with different dwelling densities or distances between the individual dwellings. These inter-dwelling distances were 10, 5 and 15 m, shown in panels (A)–(C), respectively.

external domains. Mosquitoes (both infected N and non-infected M) reside in the entire exterior domain, Ω_e, and the internal domain, Ω_i, yet are solved as distinct internal and external varieties (e.g., N_e is distinct from N_i). The internal and external mosquito variables are partitioned by the dwelling boundary along $\partial\Omega_i$ while coupled via a flux transport condition shown in Eqs. (2) and (3) along the same boundary. The exterior human variables (S_e, I_e, and R_e) reside in the external "farm" subdomain, $\Omega_f \subset \Omega_e$, and are enclosed with a Neumann insulation boundary condition along the exterior-farm boundary, $\partial\Omega_f$. Similar to the distinct mosquito variables, the internal human varieties (e.g., S_i, I_i and R_i) inhabit the dwelling domain, Ω_i, and are distinct from the exterior-farm varieties. Note that there is no coupling for the two domains of human variables; e.g., there is no flux transport term for human variables analogous to Eqs. (2) and (3).

3. Results

3.1. Equilibria of the system

We analysed system (1) to determine whether any diffusion-free steady-state solutions arise. We observe a bistable dynamic. Solving for equilibria of the non-diffusive analogue to system (1) reveals two such critical points. The first is a "trivial" or disease-free solution, which we denote P_{eq1}, with no infected mosquitoes or humans. P_{eq1} is a saddle-point and entails a straightforward dependency on the ratios of birth and death rates. For parameters in Table A1, all eigenvalues of the system for P_{eq1} are negative except one, whose corresponding eigenvector and associated geometry of the behaviour near P_{eq1} was not analysed. Numerical experiments show that any perturbation of infected mosquitoes or humans away from identically zero densities pushes solutions along the unstable trajectories surrounding P_{eq1} and drives the system towards the second critical point. The second point, denoted P_{eq2}, is a stable equilibrium reflecting an endemic infection whose eigenvalues are all negative for the parameters listed in Table A1. We further confirmed stability of P_{eq2} with numerical simulations of the full diffusive system on test geometries excluding any barriers to diffusion (e.g., complications of dwelling clusters or densities; results not shown). These equilibria are used to guide the following bulk numerical investigations, and their influence on the overall trends across solutions on the suites of geometries and their corresponding areas are apparent as noted below. See the Appendix for details on the equilibria solutions.

Numerical results of the full reaction-diffusion model equations were found with an unstructured finite element method (linear triangular discretisation), custom implemented in MATLAB and heavily vectorised for memory efficiency and performance. Geometry mesh triangularisations were built with the Sandia Laboratory–developed spatial discretiser CUBIT. A fully implicit, adaptive time integration scheme (2nd order Midpoint/BDF O(2) predictor-corrector (Gresho and Sani, 2000)) along with a

customised GMRES implementation in MATLAB solved the coupled sparse systems of linear equations. We refer the reader to Means (2010) for a detailed description of the numerical solution implementation.

3.2. Initial distributions

We applied different initial distributions of non-infected mosquitoes (external M_e) and various initial distributions of humans in the external "farm" region (susceptible S_e) over the above described suite of geometries. Initial conditions for all other variables (e.g., carrier mosquitoes, N_r, infected and recovered humans, I_r and R_r) are held the same in all domains and throughout the simulations as noted (see Table A1 for constant initial values).

External mosquito (M_e) initial distributions were at the outset a homogenous and large initial density throughout the entire external domain, Ω_e; we set M_{e0} to 1100/km^2. This was combined with a homogenous and relatively low initial infected density of $N_{e0} = 50$/km^2 to avoid leading to the trivial solution. Proximity between the human dwelling clusters and mosquito birth sites was modelled using regions where we spatially localised non-infected M_e production into a "birth zone" via the term $\Lambda_e(\vec{x})$ in system (1). $\Lambda_e(\vec{x})$ was configured to produce either a few new M_e near the dwellings (the "BZb" birth-zone) or a substantial number of M_e that are born directly on top of the cluster (e.g., the "BZd" zone; see Fig. 4).

3.2.1. Farming region human distribution

Susceptible humans, S_e, were distributed in two-dimensional Gaussian profiles centred over each farm region, with the number of distributions matching the geometry; e.g., two Gaussian distributions of humans in the two-cluster geometry or three in the three-cluster, etc. We denote this initial distribution as a "farm initial condition" or *fIC*. As the number of clusters varies in spacing, these particular initial distributions naturally overlap to differing degrees; this is illustrated in Fig. 3, where the different peak levels of the Gaussian distributions are observable. The distributions are calibrated such that we maintain the same total population density over all geometries; hence the lower maximal values as the number of clusters increase.

Fig. 5A shows transient solutions for the system on the single cluster geometry, and the strength of the initial mosquito population "burst" is evident. Within the first 10 days, rapid reactions occur in the exterior domains between the infected mosquitoes, N_e, and susceptible humans, S_e, leading to a large spike in infected people, I_e, and their eventual recovery, R_e. R_e displays the most significant spatial gradients primarily during the transient reaction phase within 100 days, well before the system relaxes to steady

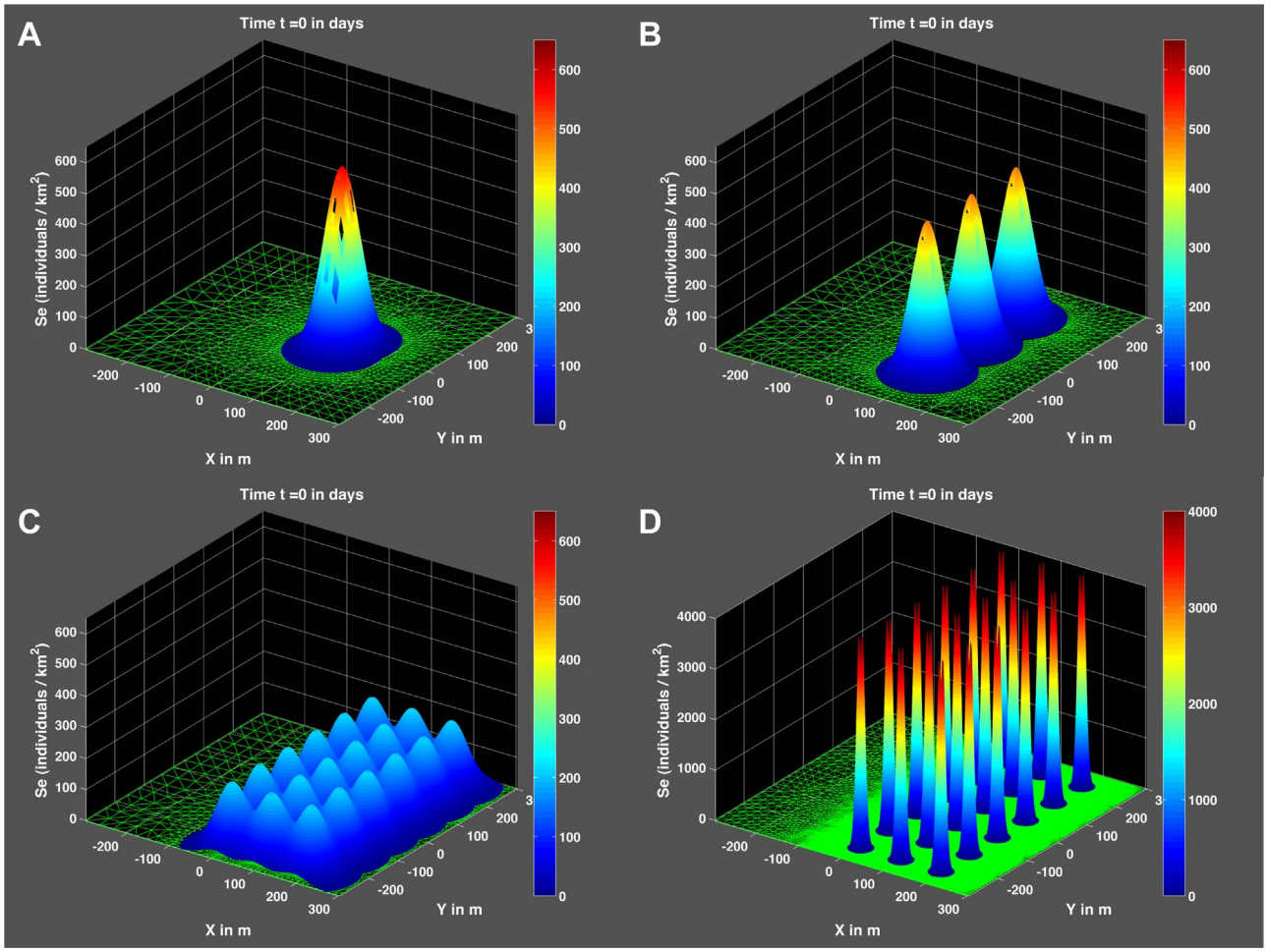

Fig. 3. Initial distributions for external "farm" susceptibles, S_e. Surface plots show the initial Gaussian profiles of human susceptible densities (individuals/km^2) aligned with the centre of each cluster distribution of "farm" regions. Here we show only three of the total five cluster geometries: one cluster (Panel A), three cluster (Panel B) and one cluster of sparsely distributed dwellings (Panel C); profiles for the two and six cluster are similar (not shown). Note the densities are adjusted across each suite of Gaussian distributions such that the overall number of individuals is constant across the geometry-cluster distribution. Panel D shows an alternate Gaussian density calibrated for an initial distribution of S_e densities tightly localised around individual dwellings instead of the entire farm region: our "dwelling-localised" initial condition, or "dIC". Similar Gaussian initial distributions are applied across all geometry-cluster combinations.

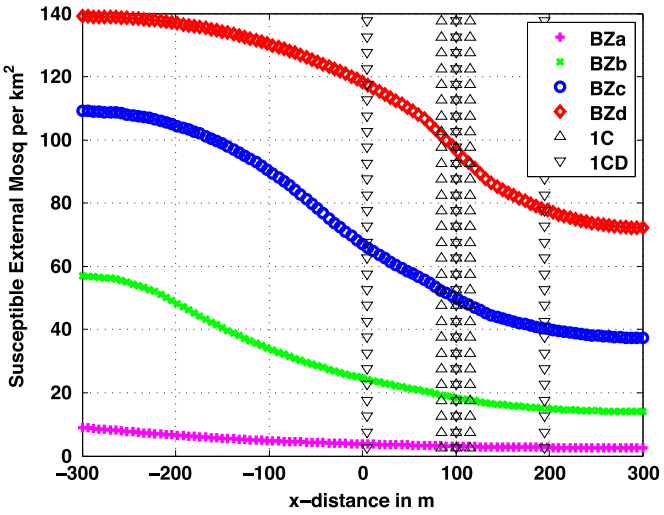

Fig. 4. Mosquito birth-zone steady states of $\Lambda_e(\vec{x})$. Four profiles are shown, demonstrating various configurations of a Heaviside-in-space, $H(\vec{x} - x_{bz})$, mosquito birthing-region distributions for our idealised geometries. Solutions are homogenous in the y-direction; hence only solutions along the x-direction are shown. Notations used are "BZ"=birth-zone combined with subscript indicating spatial extent. Here, "a" is the furthest to the left (active mosquito production in region $x \in [-300\text{ m}, x_{bz}]$ with $x_{bz} = -290$ m), "b" with $x_{bz} = -200$ m, "c" with $x_{bz} = -50$ m and "d" the furthest to the right with $x_{bz} = 100$ m). Note these profile distributions' relative proximity to each geometry cluster centred at $x = 100$ m (see Fig. 2). Vertical triangle plots indicate location of dwellings for the one-cluster (1C, 5 m interdwelling spacing) and one-cluster diffuse (1CD) geometries; note coincidence of dwellings aligned at $x = 100$ m. Combined with the constant and homogeneous death rate, μ_q, the spatially restricted birthing regions result in these steady-state profiles.

state, and reflects the Gaussian initial distribution for S_e. The gradient further exhibits some bias of the peak towards the source of mosquito births. Uninfected mosquitoes establish a steady-state gradient dictated by the birth-zone term $\Lambda_e(\vec{x})$ and the homogenous death rate, μ_q, with noticeable valleys of density around the dwelling cluster due to conversion to N_e (not shown).

Raising the levels of mosquito births around the human dwellings via extension of $\Lambda_e(\vec{x})$ to the "BZd" distribution drives S_e levels down considerably along with increases in N_e, I_e and R_e (Fig. 5B). Internal infected mosquitoes also rise substantially higher, leading to dramatically more infected individuals, I_i, at steady state, and, along with the recovered density inside the dwellings, R_i, further settle to levels exceeding the initial peak seen in the "BZb". Both I_i and R_i display spatial gradients, although not within the individual dwellings themselves but instead over the cluster of dwellings. Those more proximal to the bulk of the mosquito birth regions (e.g., $x < 100$ m) suffer higher overall infection densities than their more distant neighbours (not shown). Spatial gradients of exterior humans are dampened now with the BZd birth zone. Although R_e still displays a prominent gradient in the first 100 days, it relaxes to a modest difference of only about 5 people/km^2 at steady state.

Note that the dwelling porosity, σ_r, for our boundary transport term of Eq. (2), representing invasion of mosquitoes into the dwelling interior, is set to "high" in Fig. 5 for both sets. Lowering porosity substantially reduces all interior infection levels due to N_i densities held well under 1 individual/km^2 at steady-state for either $\Lambda_e(\vec{x})$ extents (not shown). Overall, with mosquito invasion constrained by the lower σ_r, the same relative gradients and densities result, but for the interior at far lower values than at the higher σ_r, effectively eliminating interior infections. Initial phase infections still occur, however, due to interior M_i set to 5 insects/km^2 at the outset and a non-zero N_i that rises to a density of around 20 per km^2 by 20 days. Infected humans, I_i, peak at around 1500 individuals/km^2, comparable to results with the higher porosity boundary transport. At $t=1000$ days, I_i is reduced by orders of magnitude but not eliminated and is still slowly rising to steady state. Exterior densities are only negligibly affected, as expected, and the dwelling clusters effectively act as simple diffusive barriers to transport across the farm domain.

Varying inter-dwelling distances on our suites of clustered dwelling geometries indicates a nominal effect on exterior densities while demonstrating the influence of diffusion and distribution of people. Exterior infected mosquitoes N_e are displayed over our three implemented inter-dwelling spacings of 5, 10 and 15 m on the single cluster of all 18 dwellings (see Fig. 6A). At the smallest spacing of 5 m, diffusion of mosquitoes or humans into and through the cluster appears impeded. Significantly increasing the human diffusion rate with no alteration of mosquito diffusion results in the same overall difference, depending on the distribution of S_e. With the gently sloped *flC*, the tightly clustered 5 m inter-dwelling geometry still gives lower overall densities for exterior infected mosquitoes with D_H orders of magnitude higher (Fig. 6B). Expanding the number of clusters while reducing dwelling number eliminates this effect. Only in the single cluster, and less so in the two cluster, are there enough dwellings in close proximity for such a diffusive impedance—and only during the initial transient phase of simulated time (within 20 days; not shown). Overall, essentially little to no impact of variant dwelling spacings emerges for exterior variables when comparing solution extents (e.g., max/ave/min) either at the end of simulation time (see Fig. 7) or over all time (not shown). Alternatively, confining the initial distribution of susceptible people with the "dwelling-centred" initial condition or the *dIC* (introduced next section) reverses the initial trend suggesting at least some dependency on human diffusion (Fig. 6C).

3.2.2. *Dwelling-localised human distribution*

We confined the initial Gaussian distribution of S_e to one with a much narrower base and steeper peak, the "dwelling-localised" initial condition (*dIC*) illustrated in Fig. 3D for the 1CD geometry. This *dIC* was calibrated such that total populations of external human densities are the same as in the *flC* distribution, and the smaller bases for the *dIC* Gaussian necessitate higher peaks. Out at steady state though, the *dIC* effect on all densities compared with the *flC* results is nominal, and only the *dIC* results in Fig. 7 are presented.

Due to the area dependency of the equilibrium solution, P_{eq2}, we expected independence at steady state from the initial distribution; this was further reinforced by distinctive trends emerging over the suites of geometries and their commensurate rise in area, A_r. External infection densities fall as cluster numbers rise at the presented end of simulated time (here, 1000 days). Interior infection levels are essentially flat over cluster number since the interior areas for dwellings are constant and thus not subject to variations in A_r as with the external. A trend of higher mosquito invasions with more exposed dwellings is most evident, particularly in the CD case that positions an entire column of six dwellings deeper into the mosquito birth-zone (compare dwelling locations in Fig. 4). As before with the *flC*, reducing the permeability term, σ_r, produces the same overall pattern but with dramatically lower interior densities for steady-state I_i (not shown).

Greater exposure of dwellings in the CD configuration to mosquito births also establishes the significant spatial gradient for all the interior species, which still emerge for all other configurations, yet to nowhere near the same degree. Exterior spatial distributions result for mosquitoes due to the influence of $\Lambda_e(\vec{x})$, while only negligible gradients form by comparison for humans that increase as cluster densities rise. For instance, S_e gradients are greatest for the 1C configuration and diminish to effectively

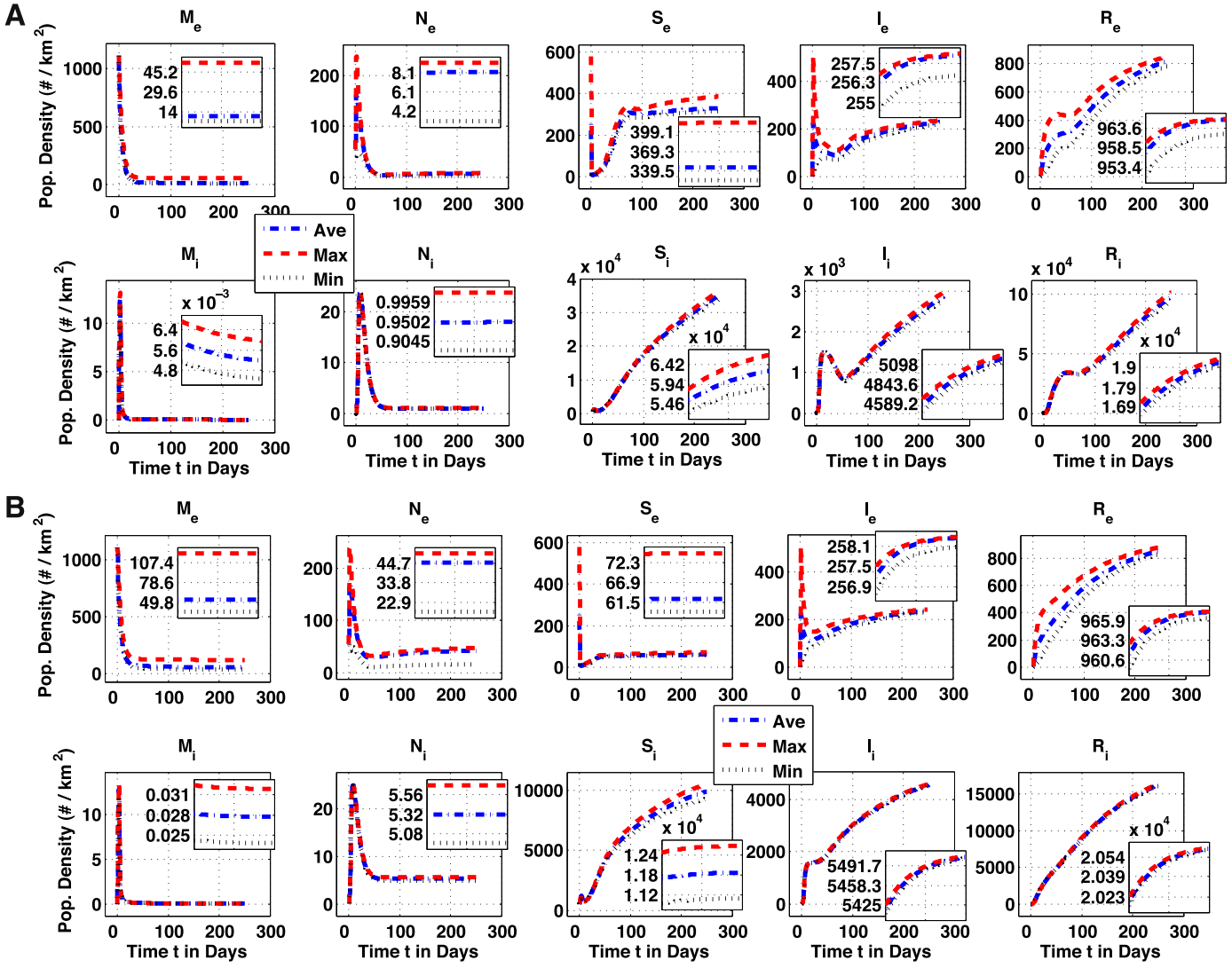

Fig. 5. Mosquito birth-zone comparison. Results here for simulations performed on the one-cluster geometry are shown, including the maximum, average and minimum values for all variables (interdwelling spacing set at 10 m). Initial non-infected mosquito density was a homogeneous and high impulse of 1100 individuals/km^2, with a homogenous and relatively low density of 50/km^2 infected N_e. Susceptible people were initially distributed according to the "farm" condition ("*flC*"), and the dwelling porosity σ_r was set to "high". Upper panels (A) are with the mosquito birth-zone set for much lower M_e production in the dwelling cluster region (notation "BZb"; see Fig. 4). Lower panels (B) are with the M_e birth-zone shifted in the positive x-direction for substantially higher densities of mosquitoes around the cluster of dwellings (notation "BZd"). Inset plots for each species are over time $t \in [650, 1000]$ days, showing systems relaxing to steady state. Initial transient solutions are quite similar within first 20 days. Out at steady state, exterior human susceptibles S_e are significantly reduced. Interior infected and recovered humans (I_i and R_i) display significant increases due to the elevated N_e. Subtler effects include stronger solution gradients (e.g., I_i and R_i) over the clusters, higher sustained densities of interior infected N_i and sharply lower exterior susceptible humans, S_e.

homogenous distributions for the CD.

Also, as suggested by results shown in Fig. 6, the inter-dwelling spacing has a limited effect on the exterior densities. Once the transient phase of the initial 20 days or so passes and solutions relax towards their respective equilibria, no significant influence of spacing dwellings from 5 up to 15 m is evident. We further tested another sparser distribution of 30 m (on the 1C configuration) with a nominal increase over the other densities—for the external variables—at steady state. Internal densities on the 30 m distribution, however, are quite different with more N_i and consequently higher I_i and R_i by around a factor of two (not shown). Note, however, that the 30 m intervals between dwellings also push the leftmost column deeper under the influence of $\Lambda_e(\vec{x})$, and I_i distributions with the 30 m spacing reflect this.

Considering again Fig. 6A and 6B, well before steady state during the initial 20-day infection phase, effects of human diffusion with the sharply confined *dIC* contrast with the *fIC*. The vastly higher diffusion rate for human transport now flips the order of infected mosquito densities over the dwelling spacings, and, with no alteration to the diffusion rate of mosquitoes, the influence of S_e on N_e emerges. The initial high peak N_e that is impeded by the 5 m spacing is driven down, and peak I_e do not rise to the same sharp initial extremes as seen in Fig. 5. Diffusion is now essentially too fast for infections to occur before peak S_e levels dissipate, and barriers such as those seen with tight 5 m spacings are overcome by such a large and non-physical rate of human "locomotion". Alternatively, impact of elevated human diffusion on internal infections is negligible as long as there are sufficient infected N_e surrounding the dwellings to invade the interior (not shown).

The trend of increasing M_i over the clusters suggested some diffusive impedance occurs with the denser dwelling configurations, and we hence tested doubling the diffusion rate of mosquitoes for the 1C variant. Steady-state levels for M_i shift to levels comparable with the 3C, and N_i rise above all other configurations except the CD. Moreover, the consistent pattern across all internal variables with larger gradients emerging as spacing increases from

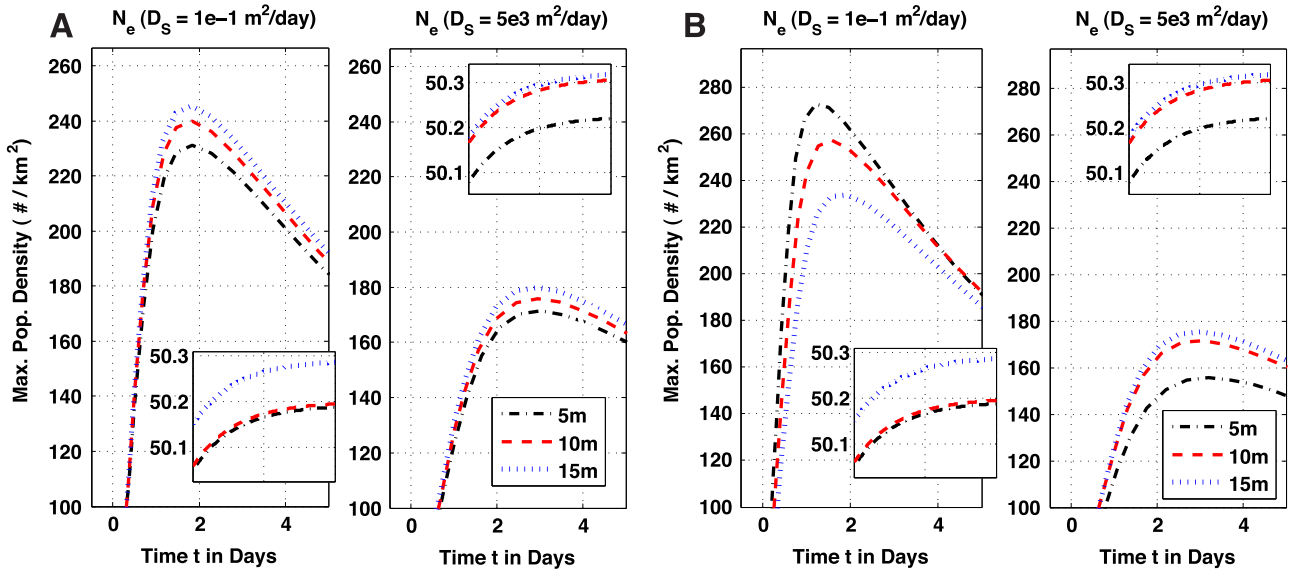

Fig. 6. Inter-dwelling distance impact. Transient solution (spatial averages) comparisons of external infected mosquitoes solo cluster geometry with varying inter-dwelling spacing (mosquito birth-zone set to "BZd", initial condition for S_e set to *flC*). Inset plots show systems relaxing to steady state over $t \in [650, 1000]$ days. Panel A shows peak exterior infected mosquito densities (N_e) with the left sub-plot results for the default diffusion rate for humans (0.1 km^2/day) and the right panel at a greatly elevated diffusion rate (5000 km^2/day). In both instances, inter-dwelling spacing effects still result in modestly higher peak levels at wider dwelling spacings. Panel B shows identical results as in Panel A, but with the "dwelling-localised" initial distribution (*dlC*) of susceptible humans for the same pair of diffusion rates (see Fig. 3). Note that the higher peak levels reflect the much steeper initial densities for S_e with the *dlC*. However, with a much faster diffusion of 5000 km^2/day, the initial trend reverses, giving a similar result to the *flC* variety where the widest spacing has the highest number of infected N_e, while the small 5 m spacing are at a lower comparable level of available N_e. At longer time scales, similar patterns emerge at the same diffusion rates, although these may be due more to numerical than distribution effects.

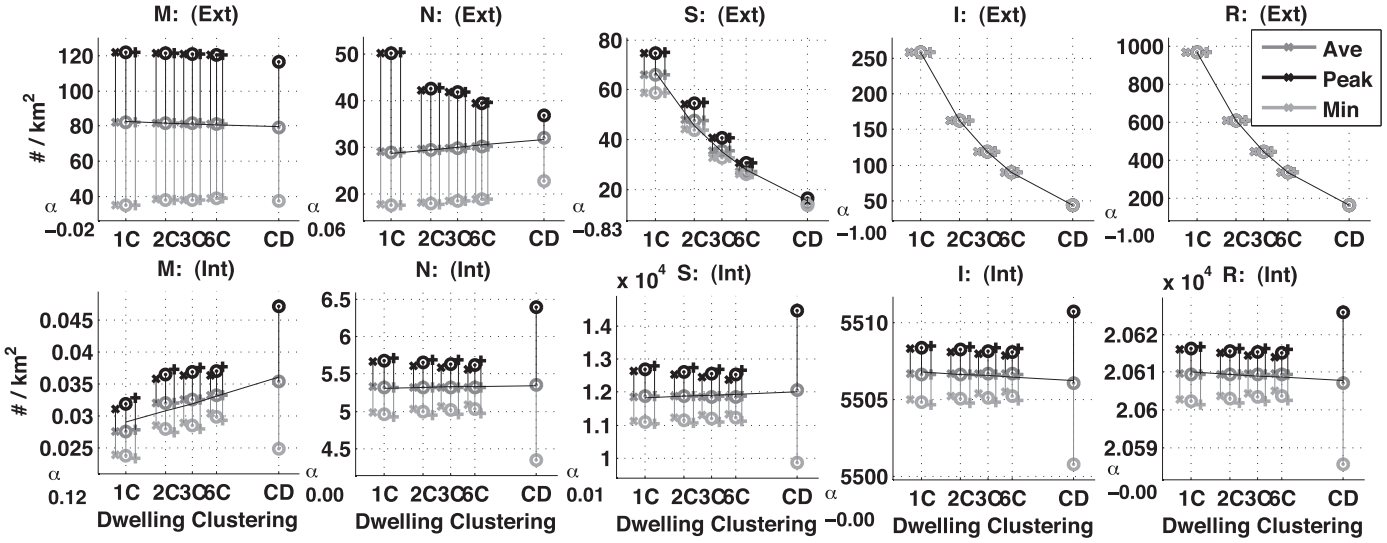

Fig. 7. Geometry impact at steady-state comparison. Solution extents (max/ave/min) over three dwelling spacings of 5, 10 and 15 m are computed at the end of simulated time, or $t = 1000$ days, over each respective spatial domain and collected for each geometric configuration. These include the one, two, three, six and the diffuse solo cluster labeled as "1C", "2C", "3C", "6C" and "CD", respectively. Distributions, initial conditions and dwelling permeabilities are identical to those given in Fig. 5B with one exception: initial S_e are now dwelling-centred, or the "*dlC*" variant (see Fig. 3). Curve fits of the form Cx^{α} to the average solutions for the intermediate 10 m dwelling spacing across all cluster configurations were computed and plotted along with their corresponding α values presented next to each subplot; parameter "C" was set to the "1C" value in each case. Residuals differ wildly, with best fit for M_i at order 0.01 to S_i with order 10^2 that improve to varying levels by excluding the "outlier" CD results. Note the logarithmic scale in the x-direction, where each column for the geometry is situated at their respective A_f area values, ranging from 0.04 to 0.2 km^2.

5 to 15 m alters with faster D_M. Mosquitoes simply more effectively penetrate the relatively dense cluster of dwellings in the 1C due to the faster diffusive transport, regardless of the interdwelling spacing. Unsurprisingly, spatial gradients are diminished for external mosquitoes, while also elevating levels of the infected N_e. This in turn drives up N_i levels as well with corresponding increases in I_i and R_i (not shown).

The emergent trend across the geometric configurations for the exterior human densities suggested fitting various functional forms to the data. We tested three varieties: simple linear ($y_0 + mx$), exponential ($Ae^{\lambda x}$) and power-law (Cx^{α}), with power-law residuals performing overall better than the other two, albeit in a relative sense, and are thus shown. Residuals are most acceptable for some variables (e.g., interior mosquitoes well under order $1e^{-4}$) but are terrible with others (e.g., S_i at order 10^2). Some improvements result from excluding the CD configuration, such as with M_e and N_e better by two orders of magnitude, yet trends are more visible with the CD variant included. Most prominent is the

near exhaustion of S_e as A_r rises up to the maximum with CD and analogous reductions of I_e and R_e. As expected, spreading out the fixed total S_e over the larger areas drives down the steady-state densities for all exterior humans. Nevertheless, the geometry impact on interior levels appears to be nominal overall and gives flat or nearly constant power-law fits. Best-fit exceptions though suggest a linear relationship with α at around -1 for exterior S_e humans and a rather less than linear α of 0.1 for internal mosquitoes, M_i.

3.3. Steady-state initial mosquito population

Results so far all initiated a burst of infection activity with a large and spatially homogeneous initial distribution of M_e throughout Ω_e. Profiles of solutions at steady state balancing the variety of spatially distributed mosquito births generated with $\Lambda_e(\vec{x})$ and the uniform death term μ_q shown in Fig. 4 were next applied as initial distributions. This reduced the initial M_e peak down to around 140 insects/km^2 at most for the "BZd" birth zone.

Such a change of initial M_e eliminates the vigorous infection event within the first 20 days, dramatically reducing peak and average mosquito densities (both internal and external). These translate into substantial changes of human densities during this initial infection phase; of particular note is the effect on the S_e reservoir. Prior results with the initial large burst of mosquitoes nearly exhausted the available S_e to infect (note the drops to nearly zero densities in Fig. 5). Now, without flooding the region with M_e and consequently N_e, more susceptible human targets survive the initial infection event, and these initial transient peaks (and valleys for S_e) of infections and recovery are less extreme than with the large burst of M_e. Out at steady state, the effects of a non-exhausted S_e reservoir appears to only modestly elevate internal densities of I and R with an otherwise negligible impact. For instance, in the 1C geometry case, both internal levels rise comparatively by around 1.4% and 1.6%, respectively ("BZb" M_e birth zone, not shown). Generally, setting the initial distribution of M_e to the distribution resulting from the balance between births and deaths lowers peak infections during the initial phase and leads to the same steady-state densities as solutions relax under the influence of P_{eq2}. Results with these dynamically balanced M_e ICs are shown in Fig. 8, as described next with spatial variations in human births.

3.4. Human birth distributions

A spatially uniform component throughout all the results thus far is homogenous human births with π independent of $\vec{x}$. We next considered the impact of introducing spatial dependency for π, distributing the births analogously to the Gaussian initial distributions, again with either a farm-centred or dwelling-centred variety. Note that S_i births were still held uniform and constant in the relatively small dwelling regions. Calibrations for each individual geometric configuration (manipulating the Gaussian profiles) to obtain comparable densities to the homogeneous external π were performed and combined with their similar initial conditions. Results were presented across these three versions in Fig. 8 for both solution extents at steady state and the transient maximums for infected I_e. For consistency, a homogeneous S_e initial distribution is included to correspond to the uniform and spatially independent π, denoted "*hIC*".

The peak levels of I_e over the first 100 days demonstrate the influence of initial distributions, with respective maximums rising from the homogenous "*hIC*" to the Gaussians and their gentle or sharp gradients with the *fIC* or *dIC*. Maximal I_e levels are highest overall for the *dIC* CD configuration, since the Gaussian ICs for S_e require such high calibrated peaks (illustrated in Fig. 3D). As cluster numbers fall down to the 1C, so do these maximum I_e with the sharp *dIC* in the first few days. For the gradually sloped *fIC* though, the 1C with its higher initial S_e elevate I_e just above the 2C levels and so forth down the configurations. Meanwhile, although difficult to see in the plot in Fig. 8A, the *hIC* show rising I_e levels that progress according to geometry. The CD hits peak levels first, then the 6C, the 3C and so on, until the longer-term dynamics take over. Eventual influence of the steady states and dependence on A_r emerges with overall similar geometric configuration progressions as with the *fIC* out to 100 days; there is some shuffling of the geometric order for the *dIC* as influence of the initial distributions fade and the steady-states begin to emerge. Note that the 1CD peak I_e falls from the highest overall initially to nearly last.

The influence of P_{eq2} and A_r is further reflected in average I_e out at steady state (plotted in Fig. 8B), where, across the IC and $\pi(\vec{x})$ combinations, increasing A_r lowers the I_e averages. Uniform π results show nearly negligible gradients that reflect the distribution of M_e more than any distribution of S_e due to the birth zone applied with $\Lambda_e(\vec{x})$—here the "BZb". Spatial variations with $\pi(\vec{x})$, however, establish rather large gradients in I_e at steady state, particularly with the dwelling-centred type. Some difficulties with numerical solutions arise for the Gaussian distributions (e.g., nearly zero densities of S_e at the farm/exterior boundary, $\partial\Omega_i$) as the cluster densities fall, forcing steeper dwelling-centred distributions. This required modifying the Gaussian calibrations to maintain S_e productions comparable to constant π; note alignments of average I_e over the configurations. Hence the anomalous variations in the extreme steady-state values of I_e, particularly the minimums, due to these distribution calibrations that incidentally demonstrate the profound influence of S_e on I_e. Either with ICs or $\pi(\vec{x})$, if the peak levels of S_e are set quite high, I_e naturally follows, and further with corresponding spatial distributions.

Instead of a falling trend, internal infections are rather flat overall (Fig. 8C). Dwelling areas are now constant across all configurations, and the steady-state solutions reflect this. Instead, I_i is now driven by the numbers of infected N_i invasions that parallel the 1C to the CD trend (not shown) and in fact mirror the "flapping flag" pattern seen in Fig. 8C. By contrast, the M_i rise over increasing cluster although at quite low densities, well less than 1 insect per km^2, and with the hIC variants showing relatively higher mosquito invasion levels until cluster densities fall to the 6C and CD (not shown). With the greater exposure by alignment of CD dwellings deeper in the $\Lambda_e(\vec{x})$, the CD still experiences highest interior infection densities.

Spatial distributions of internal infections (both insect and human) show distinct peaks in the central and/or left-most dwellings (illustrated in Fig. 10) depending on the extent of M_e births, except the CD where proximity alone to the mosquito birth zone dominates. External human births influence the formation of these interior gradients, despite uniform and constant internal π for all simulations shown. The farm- and dwelling-centred $\pi(\vec{x})$ result in rather similar extents and gradients for I_i (and N_i, not shown), while leading to different N_e clouds forming around the dwellings, reflecting the distribution of S_e; e.g., the dwelling-centred $\pi(\vec{x})$ results in N_e with higher peak levels that are more tightly confined around the cluster of dwellings (not shown).

3.5. Localised infection and breakout

Infected mosquitoes were next contained within a single dwelling—instead of homogeneously distributed throughout the exterior and interior regions—and breakout of infection observed (see Fig. 9). Numbering the dwellings starting from the upper left corner (dwelling #1) across the rows (to dwelling #3) and down to

the lower right corner (dwelling #18), we situated a high density of N_i in the "last" or 18th dwelling on order 10^2 insects/km^2. Escape rate of the interior infected mosquitoes is at the higher σ_r porosity level, and N_e densities surrounding the inaugural infection correspondingly rise—yet at a greatly diluted level in the larger Ω_f domain (order 10^{-3}). Invasion of neighbouring dwellings is somewhat delayed compared to the subsequent invasions: 10–11 days pass before the next dwelling sees any effect. Once propagated, the sequence of invasion, interior infection and escape again to the exterior progresses further, although there is still a delay in the sequence of about a day or two before any noticeable elevation of N_e surrounding a dwelling. About 3–4 days pass for peak N_i from the second to final infected dwelling for the CD geometry. The sparsely distributed CD cluster displays a relatively weak diffusive coupling between dwellings as the wave of elevated N_i densities progress up through the cluster, in contrast with results on the densely packed 1C geometry. Dwellings in the 1C are infected nearly, but not quite, in unison with about a 1 day delay of peak-to-peak across the cluster from dwelling #17 to #1—yet again after about a 10-day delay for escape of mosquitoes from the inaugural infection (not shown). In the 1C cluster, the inaugural infection again requires a roughly similar 10 days to sufficiently drive surrounding N_e levels through the σ_r term high enough to affect its neighbours' interior N_i.

At end of simulated time of 1000 days, differences between localised and concentrated infection and the extensive infections shown earlier disappear with steady-state densities across the board virtually identical. Time courses between the infection variants along the way to steady-state do differ wildly, however. Peaks of I_e, for instance, take over 60 days to emerge, unlike I_e peaks rapidly dissipating under 10 days with N_e initially everywhere (see Fig. 8A). Similar patterns result with other geometries such as the 1C showing delayed peak levels and eventually similar steady-state levels but with slightly higher infection densities (not shown).

We tried disrupting progress of the infection wave through the dwelling cluster by setting σ_r to the lower value for intervening dwellings, shown in Fig. 9A. With six of the dwellings highly resistant to N_e invasion, interior infections are delayed, with lower peak levels, but not eliminated. The more distant dwellings still experience nearly identical peak N_i at the same times as before, about 3–4 days after the second dwelling infection. Still, the "resistant" dwellings enjoy about another day before showing elevated N_i levels. With denser dwelling clusters as with the 1C, these display somewhat improved benefits of lower mosquito porosity, with delays in invasion slightly increased (not shown). Advantages of lower σ_r are far more apparent out at equilibrium (Fig. 9B). The lower porosity levels eradicate N_i, while the other dwellings experience insect levels commensurate with their exposure to the birth-zone, $\Lambda_e(\vec{x})$.

4. Discussion

Understanding the impact of spatial distributions of mosquitoes and humans on infection is crucial to understanding the dynamics of malaria. To further that aim, we have constructed a simplified general representation of human-dwelling distributions in small sub-Saharan African villages. We used five landscape or geometry variations with three different inter-dwelling spacings to investigate their influence on the dynamics of a classical susceptible-infected-recovered infectious disease-transmission model. Initial distributions of people and their influence, along with variations in mosquito and human birth distributions over the suites of geometries and impact on infection densities, were observed. Additional components—such as dwelling porosity, reflecting quality of construction, susceptibility to vector invasion and diffusive impacts—were considered. Note that this current spatial infection model is purely limited to a reaction-diffusion representation, where mosquito and human transport are treated as simple Fickian-diffusive mechanisms, and interactions between them are through classical mass-action reaction kinetics.

4.1. Human distributions and infections

We observe a dramatic effect of human distributions on infection, which is not entirely surprising given that infections do not occur without human targets. The three different types of human distributions used here, either initial conditions or births via $\pi(\vec{x})$, strongly dictate the extent of exterior infections, be they

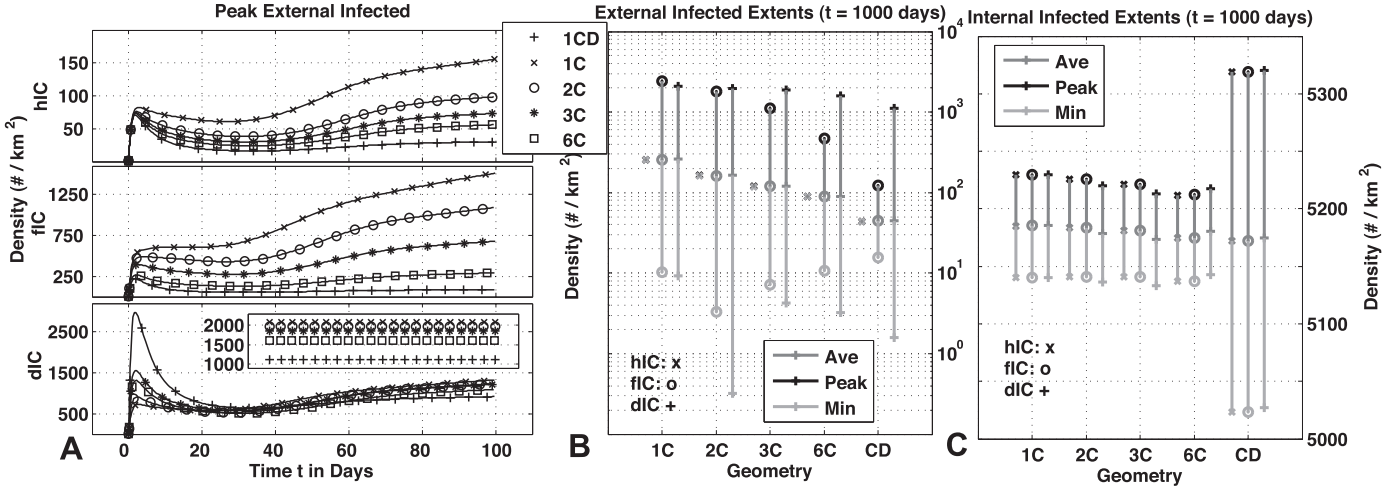

Fig. 8. Human initial condition and spatial birth distribution comparison. Three different initial human distributions—homogenous and uniform,*hIC*; farm-centred, *fIC*; and dwelling-centred, *dIC*—were combined with analogous spatially distributed human births, $\pi(\vec{x})$. Gaussian birth distributions are calibrated similarly to their IC cousins to provide the same densities of S_e as obtained with a constant π. ICs for M_e are the steady-state distributions resulting from $\Lambda_e(\vec{x})$ set to the "BZb" zone. Dwelling permeabilities are at the elevated and high σ_r, and all dwelling spacings are at the median of 10 m. Transient plots of the peak I_e presented in Panel A, with homogenous, farm- and dwelling-centred ICs and birth distributions, $\pi(\vec{x})$, across the three sub-panels are as noted for all the geometry configurations. Inset: plot for *dIC* subpanel over $t \in [800, 1000]$ days. Solution extents (max/ave/min) are plotted in Panels B and C at end of simulation time at 1000 days for the external, I_e, and internal, I_i, infections, respectively, and are aligned vertically in columns corresponding to geometry, including the three IC and $\pi(\vec{x})$ combinations. Note that the vertical scaling of Panel B is logarithmic and that labels for B and C are on the right.

homogenous or Gaussian variants. Peak initial infections clearly reflect the calibrations for the S_e initial conditions, whereas our efforts to maintain consistent total densities for S_e is evident at steady state; the averages of I_e are essentially the same across all S_e distributions (Fig. 8). Peaks and minimal I_e at steady state vary considerably, yet again mirroring the calibrations of peak and minimal human births $\pi(\vec{x})$. Alternatively, the relative consistency of internal infections across S_e distribution also reflects the homogenous distributions of S_i as well as constant areas for the dwellings, essentially equalising across geometries the influence of the area-dependent equilibrium P_{eq2}. That is, unless the impact of simple proximity to mosquito births arises as in the CD case.

Interactions between the distributions of S_e and uninfected M_e further influence formation of nearly symmetric, Gaussian-like infected mosquito "clouds" around the dwelling clusters that in turn influence I_e. Extents of these N_e clouds are quite similar for the different Gaussian IC and $\pi(\vec{x})$ combinations, despite the significant difference in steepness between them. After the first few days of infection, the homogenous S_e distributions also establish this nearly bell-shaped distribution around the clusters of dwellings, although with a gentler slope and lower peak that is shifted slightly to the left of the dwelling cluster; see Fig. 10. The N_e cloud shifting depends on the extent of mosquito births and spacing of the dwelling clusters; i.e., 5 or 15 m (see below). For the Gaussian S_e distributions, as exposure to M_e births drops from the "BZd" to the extreme "BZa" versions, the overall distribution shape remains the same yet at progressively lower densities. No shifting of the peak N_e cloud appears and is instead apparently dominated by the highly localised distribution of S_e.

The artificial yet computationally convenient restriction of human movement between the interior and exterior domains is of course partly responsible for their different trends. The only vector of infective coupling between Ω_e and Ω_i is the boundary transport of infected mosquitoes determined by σ. Hence, as long as there are sufficient mosquitoes surrounding the dwellings, internal infections result—or external, as demonstrated in Fig. 9—if σ is set high enough to permit the transport. Comparing the extreme and distant "BZa" zone results with the "BZd", external mosquito densities at steady state drop to around 1 insect per km^2, and interior M_i levels fall yet further. Nevertheless, interior infections persist at around 1/4 less but still at significant densities (averages 1300/km^2). Evidently, the most effective means of reducing interior infections, partly due to confinement of interior humans, is via a low σ that substantially dampens but does not eliminate them at steady state.

Infections are strongly determined by distributions of S_e but further influenced by the surrounding reservoir of mosquitoes to transmit infection; e.g., the extreme CD configuration situating an entire column of dwellings deeper in the range of $\Lambda_e(\vec{x})$. Further, variations of our relatively low human diffusion rate at 1.0×10^{-7} km^2 day^{-1} elicits observable effects only within the first two simulation days. Substantially faster values of D_H such as 5×10^{-3} km^2 day^{-1} lower the minimal densities of infected (external) individuals; however, after a few days, these differences all gradually disappear (Fig. 6).

4.2. Time scales of infection

The impact of varying D_H on distributions of I_e reflects the emergence of two time scales for the infection dynamics. The initial infection event, or phase one, is typically resolved by about 20 days, and phase two is the steady-state distribution when the systems relax under the influence of P_{eq2}. Overall, as expected, the IC variants demonstrate their effects only during phase one. With homogenous π, the Gaussian ICs' influence on steady-state distributions vanish, with all other elements being equal. The different inter-dwelling spacings clearly have an effect as well within the first phase of infections, and the relative impacts further depend on the transport speeds for both humans (e.g., Fig. 6) and mosquitoes. Also, when combined with different $\pi(\vec{x})$, the two time scales are apparent, yet solutions are not driven to identical densities, with peaks displaying wide variances, again demonstrating the importance of S_e distribution.

Concentrating the initial infection to a single dwelling displays these two phases of events yet varies the temporal extent of initial infections. Although the plots in Fig. 9 show interior infected mosquitoes equilibrated by 100 days, the external dynamic is still resolving (not shown). Peak infections pass by at about 60–70 days but at a substantial delay from the homogenous distribution of N_e shown in Fig. 5, where the strong initial burst of infections conclude within about 20 days. When confined to the solo dwelling and behind the filtering of a σ-controlled transport, the infection reaction takes considerably longer to propagate out and rise up to still comparable densities (about 200 I_e per km^2) as with

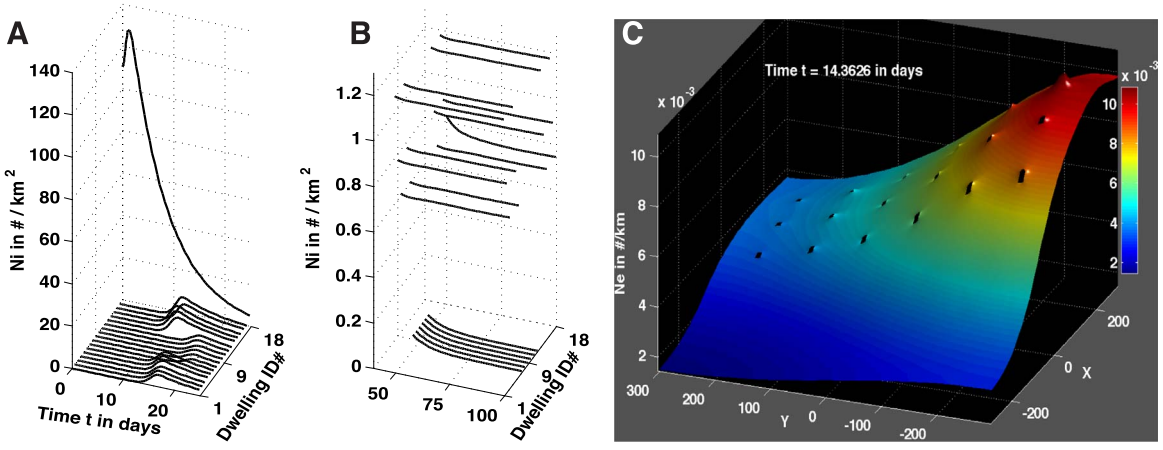

Fig. 9. Localised infected mosquito breakout. Transient plots of N_i (Panels A, B) and surface plot of N_e (Panel C) for simulation on CD geometry with localised concentration of infected mosquitoes N_i to one dwelling and essentially no infections everywhere else, including I_e and I_i. Panel A shows N_i densities over the initial 20-day infection phase within each dwelling. Numbering convention left to right, top to bottom: upper left corner dwelling #1, third dwelling upper right corner #3, etc., to dwelling #18 lower right corner, the site of initial localised infection. Dwelling porosity, σ_r, set to "high" for all dwellings except two central rows (dwellings #7 through #12) set to "low". Transient plots continued to steady state in Panel B, where different columns of dwellings and corresponding exposure to mosquito births were apparent: e.g., dwellings #1, #4, #13 and #16 had closest proximity to $\Lambda_e(\vec{x})$ with high σ_r. Exterior infected mosquito densities are plotted in Panel C; note the small scale of order 10^{-3} insects/km^2. Simulation with homogenous initial S_e ("*hIC*"), constant π and $\Lambda_e(\vec{x})$ set to the "BZb" zone.

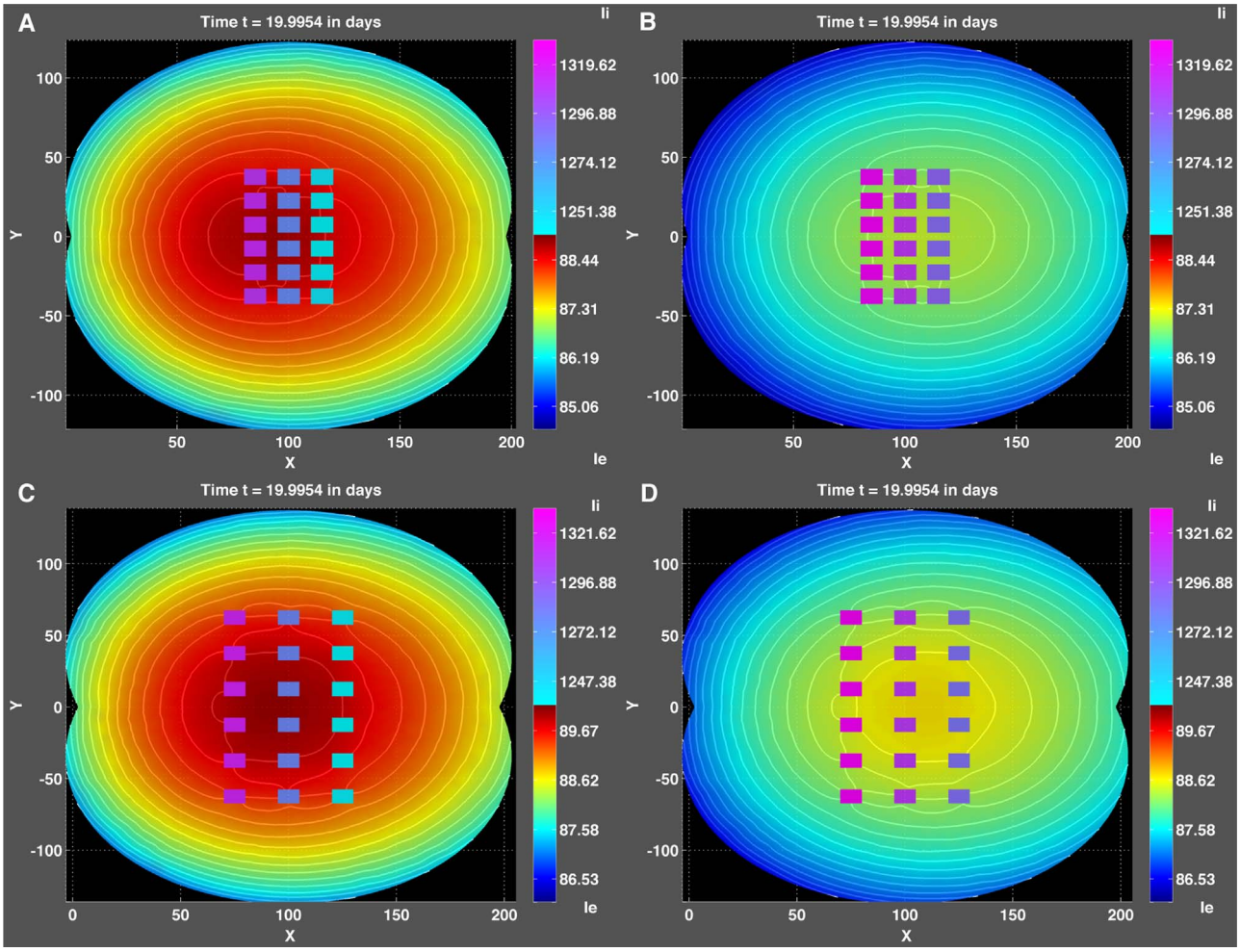

Fig. 10. Diffusion and geometry effects on infection. Contour and colour plots for simulations on 1C geometry with inter-dwelling spacing at 5 m (upper Panels A and B) and 15 m (lower Panels C and D). Initial S_e distribution set to homogeneous (*hIC*), and M_e set to an initial steady-state distribution, and source-term birth-zone placement of BZd —the greatest reach of mosquito births over the human dwellings. Panels A and C show results with baseline D_M of $8.838e^{-3}$ km^2/day (as in Table A1), whereas panels B and D are with D_M increased by a factor of 2. All panels show both external (I_e) and internal infected humans (I_i) with colour bars split into I_e (lower portion) and I_i (upper portion) showing pseudo-colour values. Note that solution ranges in upper and lower panels are distinct and set to a rather narrow range for visibility of the modest spatial variations. The impact of increased D_M is more pronounced in tight inter-dwelling spacing (upper panels) where the relative peak of I_e shifts to the right, reflecting greater penetration into the dwelling cluster. Meanwhile, the overall scale of infections remain moderately lower than with the sparse 15 m cluster.

homogeneous initial N_e but notably at a similar rapidity from minimum to peak. Once past a certain density threshold for N_e, the dynamics of the system are strongly driven from the first equilibrium P_{eq1} with zero infections to P_{eq2}. Although the rise is not quite as steep as seen for I_e in Fig. 5, the jump from almost no infections to the maximum occurs within around 40 days.

Similar results occur with homogenously distributed N_e but with a smaller overall reservoir of M_e to sustain the infection with the "BZa". A more distinctive phase one manifests than seen with "BZb" and across all combinations of IC and $\pi(\vec{x})$. Although peak densities are again higher from the *hIC* to the *dIC* variants, instead of sustained or even elevating levels above initial peaks at 100 days as in Fig. 8A, all levels fall well below 50 infections/km^2 until the attractor of P_{eq2} eventually propels infections up to steady-state levels (not shown). Hence, although a strong initial infection may establish a high peak I_e at the outset, lack of adequate supply of M_e suppresses levels of I_e. Apparently, the combination of strength of the initial infection event, its spatial distribution or confinement and persistent levels of M_e shape the extents of the initial phase. These aspects may provide more options for any intervention strategy aimed at either of the two phases.

4.3. *Influence of equilibria P_{eq1} and P_{eq2}*

Aside from the numerical challenges in resolving some of the highly stiff behaviour of the phase-one infections, the saddle point of P_{eq1} proved troublesome. Performing the isolated infections within a solo dwelling revealed the unstable dynamical trajectories emanating from P_{eq1}. Any deviation—however slight—for infected population densites from identically zero tends to drive solutions away from the "trivial" P_{eq1} towards P_{eq2}. This suggests that the unstable trajectories of P_{eq1} are aligned in the (N,I) plane. Although we did not analyse the geometry of the dynamics with associated eigenvectors and do not conclude this analytically, our numerical trials strongly suggest this. All simulations—either spatial with FEM code or non-spatial with built-in MATLAB solvers —exhibited this behaviour.

Alternatively, the dominant stability of P_{eq2} is clear, particularly with influence of regional areas, A_r. The nearly linear power-law fits ($\alpha \approx 1.0$) for exterior human variables against the nearly linear progression of increasing areas (excluding the extreme CD configuration) suggests simply spreading out the same total number of people over larger areas determines the trends observed (e.g., Fig. 7). This trend persists with simulations excluding any interior

domains, essentially evicting humans and mosquitoes from dwellings. Roughly the same progression of falling human densities as A_r rises without any geometric complications of dwelling clustering, density or inter-dwelling spacing is observed.

The increasing level of spatial gradients for S_e as cluster density rises from the CD to the 1C configuration, however, suggests other influences such as diffusive impedance of the cluster itself is also at work. Increasing the mosquito diffusion rate by a factor of two reduces the spread of extents significantly but not substantially, for the S_e densities unless we increase D_M even more or in combination with pushing D_H higher as well. With faster human diffusion, the spatial gradients can be nearly completely eliminated. At the same time, the lower levels of mosquito invasions with dwellings compacted into the 1C geometry, further enhanced by the tightest interdwelling spacing, indicates the impact of P_{eq2} is mitigated somewhat by geometry and its influence on diffusive transport.

4.4. Impact of dwelling density

We endeavored to obtain comparable exposures to the mosquito population over the geometries by aligning each suite of dwelling clusters along the same vertical axis ($x = 100$ m). An identical exposure is not quite possible though, since each individual cluster required some arbitrary organisation and orientation; e.g., the six cluster with rows of dwellings and not columns. Be that as it may, effects of mosquito diffusion emerge with these different cluster organisations where we see dwelling density across all configurations affecting internal densities. For the 1C case, since all the dwellings are the most tightly packed together, transport of mosquitoes via diffusion through the cluster is impeded; see Fig. 10.

The peaks of the N_e clouds shift closer to the "wave-front" of the mosquito birthing region. Results with the solo cluster and a homogenous S_e suggest infected mosquitoes are crowded due simply to diffusive impediments. Dwellings spread out with distances of 15 m permit shifting of the peak N_e into the cluster region itself where, interestingly, the peak value is *higher* than with the tightly compressed cluster at 5 m. This suggests that the tight clustering of dwellings function essentially as a single pseudo-dwelling, blocking penetration into the interior of the cluster. The greater exposure of the internal dwellings with less impedance (e.g., the 15 m spacings) then in turn leads to higher peak interior and exterior infections.

Across the clusters, the greater spread in infection extents for the widely spaced (15 m) dwellings indicates less diffusive coupling between the individual dwellings and the simply greater distance from the peak density of N_e. Geometric arrangements of dwellings acting as progressively less effective barriers to diffusion through the cluster regions are the primary factor for rising M_i levels across the clusters (e.g., $\alpha \approx 0.12$ in Fig. 7). Despite this, the interior infection levels are still nearly equivalent over the cluster configurations. Altering the porosity of individual dwellings within the 1C cluster—σ_r at "low" for the second row of dwellings—in an attempt to disrupt any coupling due to transport to and from the dwelling interiors has only a nominal effect on exterior or interior infections for dwellings at high σ_r at steady state (not shown). Persistence of infection levels over the cluster configurations is likely due to dominance of P_{eq2} overriding the subtle diffusive effects on M_i observed.

4.5. Diffusive impact

The interpretation above is complicated somewhat by a simple alteration to the diffusion rate of mosquitoes. Doubling the diffusion rate provided by Maidana and Yang (2007), we now see the peak I_e shift further to the right in both the tight and spread dwelling distributions (Fig. 10, Panels B and D). In itself, this is not surprising; faster diffusion results in deeper penetration by the M_e into the cluster where in fact the greatest densities of N_e and thus I_e are now on the lee of the dwellings downwind from the mosquito wavefront. However, the levels of human infections are altered, with the internal rising and external falling. Higher I_i is mostly due to greater penetration of N_e into the dwelling cluster, whereas lower I_e reflects the relative time scales for diffusion and infection. With diffusion now twice as fast and a corresponding diffusion length (via $L = 2\sqrt{Dt}$, with $t=1$ day) of roughly 270 m, the reaction time for mosquito infections of $\beta_m = 0.05$/day or even the human at $\beta_h = 0.5$/day (see system (1)) is simply not fast enough to keep up with the mosquitoes diffusing away. Furthermore, this is with dwellings also impeding mosquito diffusion through the cluster at various impacts with tight or spread out clusters. If, for some reason, however, the N_e densities, or S_e for that matter, are sufficiently high (of the order 10^3 individuals/km^2, say), then infective reactions would dominate before diffusive effects could drive the mosquitoes away. This may indeed be the case in high S_e population areas not under consideration here.

Alternatively, varying the infection rates while holding the baseline D_M fixed, we can shift the peak N_e to the right or left as we wish. Slower β values move the peak through the cluster to the right—reflecting the longer time required for infections to keep up with diffusion—while faster β achieves the reverse (not shown). Perhaps of greatest interest here, however, is the impact of the increased diffusion rate on the levels of N_e and infected humans, I_e and I_i. With the faster diffusion for mosquitoes, despite the greater penetration into the cluster and corresponding greater exposure of people, the infected levels are lower.

4.6. Limitations

The above discussion on diffusive effects highlights a clear limitation in this study. Diffusion is by no means the only transport mechanism at work in the lives of mosquitoes and humans. Our intention, however, was to expand the prior spatial study to consider more complex arrangements of dwellings, clusters of dwellings and asymmetric mosquito and human distributions on relatively small landscapes such as those seen in rural communities of Fig. 1. Thus important aspects of mosquito transport, such as advection or wind effects, were neglected (Al-Arydah and Smith?, 2011). Given cruising speeds of mosquitoes at around 0.7 m/s (Snow, 1976) that can traverse our landscape geometry within an hour, we instead focused solely on diffusive transport at this phase of the model. Nevertheless, imposition of a vector field driving mosquitoes either to or away from a cluster of dwellings may dramatically affect the results, as suggested by the discussion of relative time scales for diffusion and infection.

Further, the strong impact of human distributions demonstrates that modelling efforts aimed at characterizing infectious dynamics in any spatial context requires careful representation of human activity. Where the humans are and how they move about dictates the patterns and levels of exterior infection regardless, as suggested by the relatively simple human distributions employed here. Limitations include our artificial demarcation of people into interior and exterior varieties, with no transport between them, that fails to capture essential components of human behaviour (e.g., daily movements from residential to farming or commercial regions) as well as aggregations of people against concentration gradients (e.g., gatherings at festivals, etc.). Moreover, we have not considered any intervention methods such as interior residual spraying or larval controls, instead choosing to focus on the subtle complexities of human and mosquito distributions and density

interactions alone.

The troublesome aspects of the P_{eq1} saddle point complicated our efforts. Simulations set with zero infections everywhere, either mosquito or human, eventually experience an infection event of the phase-one type: a rapid transition from minimal to peak infections once densities of N_e pass a certain threshold. This is due to the very nature of numerical simulations; setting initial conditions to identically zero is certainly possible, but numerical errors on the order of machine-ϵ that are typically perfectly acceptable for generic applications here fail due to the influence of the P_{eq1} saddle. The second-order BDF applied for these simulations presented similar results to trials with non-diffusive ODE solutions in MATLAB (ode15s, rel/abs tolerances of $1e^{-6}$ and lower) and hence limited these spatial explorations to those that avoid initial distributions with zero infections.

5. Conclusions

Although numerically troublesome, the dynamics of the system established by P_{eq1} driving infections to P_{eq2} and the inherently dual-phase temporal dynamics for the continuum SIR model employed here suggest any tactics of intervention must consider the phase of infection. Initial phase behaviour is distinguished by dramatic elevations of infection evolving on much shorter time scales clearly calibrated by intensity and distribution of inaugural infection, and rapid response within days may be essential. Over the longer secondary phase as P_{eq2} dominates, speed of response may not be so critical instead of simple persistent efforts to eradicate the M reservoir or just isolating N and I densities from traversing the unstable trajectories around P_{eq1}. Either way, results here confirm the approaches of quarantine (e.g., low σ), distance (e.g.,"BZa" $\Lambda_e(\vec{x})$) and ideally eradication of vectors that are so intuitively apparent without modelling effort.

A key result from our work, however, is that tightly compressed dwellings result in high peak levels when diffusion is low, but these can be reduced when diffusion is fast. Thus dwellings that cluster in windy areas, for instance, may not be as much at risk as those that cluster in non-windy regions if we consider diffusion alone a reasonable representation of mosquito transport. This will help guide intervention strategies based on geography. Such considerations should likely include the simple proximity to birth sites of mosquitoes that directly influence levels of infection; however, this is complicated by human densities and distributions. Successful larval control methods may then require substantial levels of intervention given the complexities noted here and elsewhere for spatial and temporal distributions of birthing regions (Githeko et al., 2012). Additionally, the effects of dwelling porosity or quality of home construction suggest that reducing susceptibility of homes to mosquito invasion alone may potentially eliminate exposure of people to infection, at least indoors. This is conditional of course on practical caveats of when and whether people stay indoors as well as the economic feasibility for increased housing quality.

A note of caution is warranted, however. The relative ease and convenience of expanding classic SIR dynamics to include spatial components with reaction-diffusion effects as we have done here, and the flexibility permitted with FEM approaches, comes with tradeoffs. Continuum approximations such as simulating less than one insect per km^2 that nevertheless leads to widespread infection events due to the influence of the model's equilibria (and numerical realities) suggest discrete spatial methods may be more suitable. The highly sensitive and unstable trajectories along the (N,I) plane requires careful handling to omit spurious events from machine-ϵ-sized infections. Further, impedance of mosquito invasions through apertures of 5 m also indicate scaling issues for the diffusive representation; it is not likely a 1 cm insect is intimidated by such obstacles. Diffusive models for human behaviour also gloss over the complexities and subtleties driving concentration or dispersion of the clearly all-important distributions of S that in turn dictate the infection extents as seen here.

The overarching importance of human distributions, their transport and interaction with infectious "clouds" of mosquitoes on the infection dynamic must therefore guide any future spatial modelling efforts. Incorporating intervention methods (e.g., IRS, mosquito bed nets, etc.) including spatial heterogeneities and advective effects on mosquitoes could be founded on a discrete representation of human distributions and movements, perhaps an agent-based model on a discrete grid or Monte Carlo walk through a graph network. Proper handling of any unstable "trivial" and uninfected states would be essential. Such a scheme could still benefit from the relative ease of a diffusion model such as chemical attractant gradients for mosquitoes. Regardless, the dominant impact of human distributions clearly requires substantial care in any spatial modelling effort investigating infection dynamics.

Acknowledgements

SAM would like to express his gratitude to the Auckland Bioengineering Institute of the University of Auckland for supporting this work. RJS? is supported by an NSERC Discovery Grant. For citation purposes, note that the question mark in "Smith?" is part of his name.

Appendix A. Equilibria

For system (1), we wish to find any equilibria of the associated non-diffusive analogue and do so by exploiting the symbolic package Maple. For simplicity of this derivation, we treat the different area terms of the system (A_e, A_r and A_β) as the same for an idealised geometric region. We obtain two equilibrium points, one of which is the disease-free equilibrium, denoted P_{eq1}, with infected mosquitoes and humans at zero density:

$$S_{eq1} = \frac{\pi}{\mu_h A} = \frac{9125}{A}$$
$$I_{eq1} = 0$$
$$R_{eq1} = 0$$
$$M_{eq1} = \frac{\Lambda_e}{\mu_q A} = \frac{20.002}{A}$$
$$N_{eq1} = 0.$$

We see dependence of this first equilibrium point on the ratios of birth and death rates as well as scaling by unit area for variables in densities of *individuals*/L^2. Using the next-generation method, we estimate the basic reproduction number at the disease-free equilibrium via the incidence of infection and dwell time of infection:

$$R_0 = \sqrt{\frac{A_\beta \beta_h S_{eq1} \cdot A_\beta \beta_m M_{eq1}}{\mu_q (h + \alpha + \mu_h + \gamma)}}.$$

For simplicity here with the non-diffusive case, we treat the areas such as A_β as 1. Hence, we obtain $R_0 = 40.57$ using the default parameters given in Table A1.

Table A1
Parameter values.

Parameter	Description	Value	Reference
D_M	Mosquito diffusion (All Ω)	8.838×10^{-3} km^2 day^{-1}	Maidana and Yang (2007)
D_H	Human diffusion (All Ω)	1.0×10^{-7} km^2 day^{-1}	Estimated
A_r,A_e	Area (farm, exterior)	Geometry dependent; km^2	Calculated
A_β	Infection rate area scaling	100×100 m^2	Estimated
Λ_e	Mosquito birth rate	1000 year^{-1}	Al-Arydah and Smith? (2011)
$\Lambda(\vec{x})$: BZa	Mosquito birth zone "a"	$x \leq -290$ m	
$\Lambda(\vec{x})$: BZb	Mosquito birth zone "b"	$x \leq -200$ m	
$\Lambda(\vec{x})$: BZc	Mosquito birth zone "c"	$x \leq -50$ m	
$\Lambda(\vec{x})$: BZd	Mosquito birth zone "d"	$x \leq 100$ m	
μ_q	Mosquito death rate	7.3^{-1} day^{-1}	Al-Arydah and Smith? (2011)
β_m	Mosquito infection rate	0.05 human^{-1} day^{-1}	Al-Arydah and Smith? (2011)
π	Human birth rate	1/2 humans day^{-1}	Al-Arydah and Smith? (2011)
β_h	Human infection rate	0.5 mosq^{-1} day^{-1}	Al-Arydah and Smith? (2011)
h	Human I → S rate	1/9 day^{-1}	Al-Arydah and Smith? (2011)
δ	Human R → S rate	1/30 day^{-1}	Al-Arydah and Smith? (2011)
μ_h	Human death rate	1/18250 day^{-1}	Al-Arydah and Smith? (2011)
α	Human I → R rate	1/8 day^{-1}	Al-Arydah and Smith? (2011)
γ	Human I death rate	0.05 day^{-1}	Al-Arydah and Smith? (2011)
σ_r	Dwelling porosity (high)	0.8 mosq. m^{-1} day^{-1}	Estimated
σ_r	Dwelling porosity (low)	1×10^{-3} mosq. m^{-1} day^{-1}	Estimated
M_{e0} and M_{i0}	Mosquito M IC (homogeneous)	1100 and 50 mosq./km^2	Estimated
N_{e0} and N_{i0}	Mosquito N IC (homogeneous)	50 and 0.01 mosq./km^2	Estimated
S_{e0} and S_{i0}	Human S IC (homogeneous)	100 and 500 humans/km^2	Estimated
I_{e0} and I_{i0}	Human I IC (homogeneous)	0.01 humans/km^2	Estimated
R_{e0} and R_{i0}	Human R IC (homogeneous)	0.01 humans/km^2	Estimated

The second, endemic, equilibrium point P_{eq2} exhibits a more complicated dependency on the parameters of the system. We show "compact" versions here:

$$S_{eq2} = \frac{1}{A\beta_M}\frac{\mu_q(h+\alpha+\mu_h+\gamma)\left(\left(b\mu_h+\gamma\delta+\mu_h^2\right)\mu_q+p\beta_M\delta+p\beta_M\mu_h\right)}{\left(\mu_h^3+a\mu_h^2+c\mu_h\right)\mu_q+\beta_h\mu_h^2\lambda+\beta_h\lambda b\mu_h+\beta_h\delta\gamma\lambda}$$

$$I_{eq2} = -\frac{1}{A\beta_M}\frac{\left(\left(\mu_h^2+(h+\alpha+\gamma)\mu_h\right)\mu_q^2-\beta_h\lambda p\beta_M\right)(\delta+\mu_h)}{\left(\mu_h^3+a\mu_h^2+c\mu_h\right)\mu_q+\beta_h\mu_h^2\lambda+\beta_h\lambda b\mu_h+\beta_h\delta\gamma\lambda}$$

$$R_{eq2} = -\frac{1}{A\beta_M}\frac{\alpha\left(\left(\mu_h^2+(h+\alpha+\gamma)\mu_h\right)\mu_q^2-\beta_h\lambda p\beta_M\right)}{\left(\mu_h^3+a\mu_h^2+c\mu_h\right)\mu_q+\beta_h\mu_h^2\lambda+\beta_h\lambda b\mu_h+\beta_h\delta\gamma\lambda}$$

$$M_{eq2} = \frac{1}{A\beta_h}\frac{\left(\mu_h^3+a\mu_h^2+c\mu_h\right)\mu_q+\beta_h\mu_h^2\lambda+\beta_h\lambda b\mu_h+\beta_h\delta\gamma\lambda}{\left(\left(b\mu_h+\gamma\delta+\mu_h^2\right)\mu_q+p\beta_M\delta+p\beta_M\mu_h\right)}$$

$$N_{eq2} = -\frac{1}{A\beta_h}\frac{\left(\left(\mu_h^2+(h+\alpha+\gamma)\mu_h\right)\mu_q^2-\beta_h\lambda p\beta_M\right)(\delta+\mu_h)}{\left(\left(b\mu_h+\gamma\delta+\mu_h^2\right)\mu_q+p\beta_M\delta+p\beta_M\mu_h\right)\mu_q}.$$

We streamlined these expressions with the following simplifying relations

$$a = (h+\alpha+\delta+\gamma)$$
$$b = (\delta+\alpha+\gamma)$$
$$c = \delta(\alpha+h+\gamma).$$

The above expressions simplify to the following values, all scaled by the idealised area A using the default system parameter values given in Table A1:

$$S_{eq2} = \frac{0.363}{A}$$
$$I_{eq2} = \frac{9.95}{A}$$
$$R_{eq2} = \frac{37.2}{A}$$
$$M_{eq2} = \frac{4.32}{A}$$
$$N_{eq2} = \frac{15.7}{A}.$$

Numerical results confirm these values both with a simple region with $A=1$ and for a variety of geometry areas; however, it should be noted that, for the suite of six geometries tested, the areas are more complicated due to different regions of activity for mosquitoes (the entire external region A_e) or humans (the "farming" regions A_r), and numerically obtained results reflect these variations. Of further note is dependence of equilibria on the birth rates for mosquitoes, $\Lambda(\vec{x})$, which is also subject to alterations by virtue of spatial distributions; e.g., the "BZx" birthing zone variants.

Linearisation of these equilibria was performed and stability classified—for the parameter values listed in Table A1—again in Maple. Associated eigenvectors and geometry of the dynamics was not analysed. All eigenvalues for P_{eq2} are negative, and hence it is a stable critical point. P_{eq1}, however, includes one positive eigenvalue amongst a suite of otherwise negative eigenvalues and is thus a saddle point. The largest eigenvalue for P_{eq1} is given by:

$$\lambda_{max}^{P_{eq1}} = -\frac{1}{2\mu_h\mu_q}\left\{\mu_h\mu_q^2+\left(\mu_h^2+[\gamma+\alpha+h]\right)\mu_q+\sqrt{\Delta}\right\}$$

$$\Delta = \mu_h^2\mu_q^4-2\left(\mu_h^3+[\gamma+\alpha+h]\mu_h^2\right)\mu_q^3+\left\{\mu_h^4+2[\gamma+\alpha+h]\mu_h^3+\left[\gamma^2+\alpha^2+h^2+2\alpha\gamma+2\gamma h+2\alpha h\right]\mu_h^2\right\}\mu_q^2+4\pi\beta_h\beta_m\lambda\mu_h\mu_q. \quad \text{(A.1)}$$

Default parameter values result in an eigenvalue of about 67.3 for $\lambda_{max}^{P_{eq1}}$. A simple sampling of the parameter space aimed at reducing the radical term Δ in expression (A.1) and producing a stable disease-free equilibrium indicates greatest sensitivity to μ_q, the mosquito death rate. Increases by two orders of magnitude for μ_q drives $\lambda_{max}^{P_{eq1}}$ below zero, whereas other parameters require substantially larger modifications when altered alone. Reducing mosquito births (Λ) by an order of magnitude in tandem with μ_q lowers the required rise in mosquito deaths to produce this effect.

Although a thorough bifurcation analysis is beyond the scope of this paper, it appears a semi-pitchfork bifurcation occurs with rising μ_q, transitioning the system from two equilibria (an unstable disease-free equilibrium and a stable endemic equilibrium) to a single, stable disease-free equilibrium. Hence, considering $\lambda_{max}^{P_{eq1}}$ as a representative threshold for the basic reproductive ratio for a non-diffusive analogue of system (1), we have $R_0 > 1$ for default

parameters unless mosquito deaths (or births, say) are modified enough to transition $\lambda_{max}^{P_{eq1}} < 0$ and hence $R_0 < 1$.

Numerical tests of this non-diffusive analogue with MATLAB ODE solvers (e.g., ode15s) confirm unstable trajectories emanate from P_{eq1} but appear confined to directions along the (N,I) plane. Identically zero initial conditions for N or I remain fixed at P_{eq1} given caveats of suitable relative and absolute error handling. If machine-ϵ ICs for N or I are used, however, eventually infections rise and follow trajectories traversing from P_{eq1} to P_{eq2}. Simulations with modified mosquito deaths are consistent with expectations regarding the impact on $\lambda_{max}^{P_{eq1}}$: the endemic equilibrium merges with the disease-free equilibrium as μ_q rises, and we obtain a stable disease-free system for sufficiently large increases in μ_q. The relatively high sensitivity to μ_q in our model suggests that interventions may be most effective when directed at eradication of the mosquito vector.

References

Al-Arydah, M., Smith?, R., 2011. Controlling malaria with indoor residual spraying in spatially heterogenous environments. Math. Biosci. Eng.: MBE 8 (4), 889–914. http://dx.doi.org/10.3934/mbe.2011.8.889.

Alyward, B., Hennessey, K., Zagario, N., Olivé, J., Cochi, S., 2000. When is a disease eradicable? 100 years of lessons learned. Am. J. Public Health, 1515–1520.

Breman, J.G., Alilio, M.S., Mills, A., 2004. Conquering the intolerable burden of malaria: what's new, what's needed: a summary. Am. J. Trop. Med. Hyg. 71 (Suppl 2), 1–15.

Carson, R., 1962. Silent Spring. Houghton Mifflin.

Carter, R., Mendis, K.N., Roberts, D., 2000. Spatial targeting of interventions against malaria. Bull. World Health Organ. 78 (12), 1401–1411.

Fillinger, U., Ndenga, B., Githeko, A., Lindsay, S.W., 2009. Integrated malaria vector control with microbial larvicides and insecticide-treated nets in western Kenya: a controlled trial. Bull. World Health Organ. 87, 655–665.

Ghebreyesus, T., Haile, M., Witten, K., Getachew, A., Yohannes, M., Lindsay, S., Byass, P., 2000. Household risk factors for malaria among children in the Ethiopian highlands. Trans. R. Soc. Trop. Med. Hyg. 94, 17–21.

Githeko, A.K., Ayisi, J.M., Odada, P.K., Atieli, F.K., Ndenga, B.A., Githure, J.I., Yan, G., 2006. Topography and malaria transmission heterogeneity in western Kenya highlands: prospects for focal vector control. Malar. J. 5, 107. http://dx.doi.org/10.1186/1475-2875-5-107.

Githeko, A.K., Ototo, E.N., Guiyun, Y., 2012. Progress towards understanding the ecology and epidemiology of malaria in the western Kenya highlands: opportunities and challenges for control under climate change risk. Acta Trop. 121 (1), 19–25. http://dx.doi.org/10.1016/j.actatropica.2011.10.002.

Gresho, P., Sani, R., 2000. Incompressible Flow and the Finite Element Method. John Wiley and Sons, Ltd., Chichester.

Hasibeder, G., Dye, C., 1988. Population dynamics of mosquito-borne disease: persistence in a completely heterogeneous environment. Theor. Popul. Biol. 33 (1), 31–53.

Hasibeder, G., Dye, C., 1988. Population dynamics of mosquito-borne disease: persistence in a completely heterogeneous environment. Theor. Popul. Biol. 33, 31–53.

Keiser, J., Utzinger, J., de Castro, M.C., Smith, T.A., Tanner, M., Singer, H., 2004. Burton, Urbanization in sub-Saharan Africa and implication for malaria control. Am. J. Trop. Med. Hyg. 71 (2), 118–127.

Kierstead, H., Slobodkin, L.B., 1953. The size of water masses containing plankton blooms. J. Mar. Res. 12 (1), 141.

Killeen, G.F., Seyoum, A., Sikaala, C., Zomboko, A.S., Gimnig, J.E., Govella, N.J., White, M.T., 2013. Eliminating malaria vectors. Parasit. Vectors 6, 172. http://dx.doi.org/10.1186/1756-3305-6-172.

Lopez, A.D., Mathers, C.D., Ezzati, M., Jamison, D.T., Murray, C.J.L., 2006. Global and regional burden of disease and risk factors, 2001: systematic analysis of population health data. Lancet 367 (9524), 1747–1757. http://dx.doi.org/10.1016/S0140-6736(06)68770-9.

Macintyre, K., Keating, J., Okbaldt, Y.B., Zerom, M., Sosler, S., Ghebremeskel, T., Eisele, T.P., 2006. Rolling out insecticide treated nets in Eritrea: examining the determinants of possession and use in malarious zones during the rainy season. Trop. Med. Int. Health 11 (6), 824–833. http://dx.doi.org/10.1111/j.1365-3156.2006.01637.x.

Maidana, N., Yang, H., 2007. A spatial model to describe the dengue propagation. TEMA-Tend. Mat. Apl. 8, 83–92.

Means, S.A., 2010. Spatio-temporal calcium dynamics of the interstitial cells of Cajal (Ph.D. dissertation), University of Auckland, ⟨http://hdl.handle.net/2292/6117⟩.

Murray, C.J.L., Rosenfeld, L.C., Lim, S.S., Andrews, K.G., Foreman, K.J., Haring, D., Fullman, N., Naghavi, M., Lozano, R., Lopez, A.D., 2012. Global malaria mortality between 1980 and 2010: a systematic analysis. Lancet 379, 413–431. http://dx.doi.org/10.1016/S0140-6736(12)60034-8.

Silué, K.D., Raso, G., Yapi, A., Vounatsou, P., Tanner, M., N'goran, E.K., Utzinger, J., 2008. Spatially-explicit risk profiling of plasmodium falciparum infections at a small scale: a geostatistical modelling approach. Malar. J. 7, 111. http://dx.doi.org/10.1186/1475-2875-7-111.

Smith?, R., Hove-Musekwa, S., 2008. Determining effective spraying periods to control malaria via indoor residual spraying in sub-Saharan Africa. J. Appl. Math. Decis. Sci. 2008, Article ID 745463.

Snow, R.W., Guerra, C.A., Noor, A.M., Myint, H.Y., Hay, S.I., 2005. The global distribution of clinical episodes of plasmodium falciparum malaria. Nature 434 (7030), 214–217. http://dx.doi.org/10.1038/nature03342.

Snow, W., 1976. The direction of flight of mosquitoes (diptera, culicidae) near the ground in west African Savanna in relation to wind direction, in the presence and absence of bait. Bull. Entomol. Res. 65, 555–562.

Zhou, G., Munga, S., Minakawa, N., Githeko, A.K., Yan, G., 2007. Spatial relationship between adult malaria vector abundance and environmental factors in western Kenya highlands. Am. J. Trop. Med. Hyg. 77 (1), 29–35.